Inverted selective plane illumination microscopy (*i*SPIM) enables coupled cell identity lineaging and neurodevelopmental imaging in *Caenorhabditis elegans*

Yicong Wu[a,1], Alireza Ghitani[a], Ryan Christensen[b], Anthony Santella[c], Zhuo Du[c], Gary Rondeau[d], Zhirong Bao[c,2], Daniel Colón-Ramos[b,2], and Hari Shroff[a,2]

[a]Section on High Resolution Optical Imaging, National Institute of Biomedical Imaging and Bioengineering, National Institutes of Health, Bethesda, MD 20892; [b]Program in Cellular Neuroscience, Neurodegeneration and Repair, Department of Cell Biology, Yale University School of Medicine, New Haven, CT 06536; [c]Developmental Biology Program, Sloan–Kettering Institute, New York, NY 10065; and [d]Applied Scientific Instrumentation, Eugene, OR 97402

Edited* by Jennifer Lippincott-Schwartz, National Institutes of Health, Bethesda, MD, and approved September 20, 2011 (received for review May 26, 2011)

The *Caenorhabditis elegans* embryo is a powerful model for studying neural development, but conventional imaging methods are either too slow or phototoxic to take full advantage of this system. To solve these problems, we developed an inverted selective plane illumination microscopy (*i*SPIM) module for noninvasive high-speed volumetric imaging of living samples. *i*SPIM is designed as a straightforward add-on to an inverted microscope, permitting conventional mounting of specimens and facilitating SPIM use by development and neurobiology laboratories. *i*SPIM offers a volumetric imaging rate 30× faster than currently used technologies, such as spinning-disk confocal microscopy, at comparable signal-to-noise ratio. This increased imaging speed allows us to continuously monitor the development of *C, elegans* embryos, scanning volumes every 2 s for the 14-h period of embryogenesis with no detectable phototoxicity. Collecting ∼25,000 volumes over the entirety of embryogenesis enabled in toto visualization of positions and identities of cell nuclei. By merging two-color *i*SPIM with automated lineaging techniques we realized two goals: (*i*) identification of neurons expressing the transcription factor CEH-10/Chx10 and (*ii*) visualization of their neurodevelopmental dynamics. We found that canal-associated neurons use somal translocation and amoeboid movement as they migrate to their final position in the embryo. We also visualized axon guidance and growth cone dynamics as neurons circumnavigate the nerve ring and reach their targets in the embryo. The high-speed volumetric imaging rate of *i*SPIM effectively eliminates motion blur from embryo movement inside the egg case, allowing characterization of dynamic neurodevelopmental events that were previously inaccessible.

fast 4D imaging | axon growth | neuron migration

Proper neural circuit assembly requires the coordinated execution of multiple events, including cell migration, axon guidance, and synaptogenesis (1, 2). During neurodevelopment, these events are orchestrated between pre- and postsynaptic partners, resulting in the correct wiring of the nervous system. The mechanisms that enable proper wiring in vivo are not well understood.

Caenorhabditis elegans provides an excellent model to understand how neural circuit assembly occurs in vivo. With only 302 neurons, ∼7,000 synapses, and an available and comprehensive neural connectivity map (3), the nervous system of *C. elegans* is well characterized and relatively simple. The molecular mechanisms that control neurodevelopmental decisions in the nematode are well conserved throughout evolution (4), and several genetic programs that control terminal differentiation of neuronal identity were first identified and characterized in *C. elegans* (5, 6). Studies in *C. elegans* have also significantly contributed to our understanding of neuroblast migration and axon guidance (7, 8). One of the model experimental systems for studying neuroblast migration in nematodes is the pair of canal-associated neurons (CANs) (9–17). Identification of the molecules required for CAN migration also revealed conserved genetic programs required for cellular migration in vertebrates (18, 19). Moreover, the conserved Netrin signaling pathway and its associated receptors (UNC-40/DCC and UNC-5) were first discovered in *C. elegans* (20–22). In these studies, in vivo labeling and visualization of nematode neurites facilitated identification of downstream molecular factors required for Netrin-dependent guidance (23).

Though genetic studies in *C. elegans* have revealed the identity of the molecular players required for neurodevelopment, the mechanisms by which conserved genetic programs direct neural circuit formation during embryonic neurulation are less understood. Most neurodevelopmental studies have been conducted in fixed embryos or as end-point genetic analyses in nematode larvae. Real-time inspection of neurulation in the embryo would be of great value in visualizing the neurodevelopmental dynamics that allow innervation of the nematode nervous system. However, directly observing neurodevelopment in the embryo has proven difficult because of fast movement and twitching of the embryo inside the egg shell. Removing this rapid motion with anesthetics is impractical because of the relatively impermeable nature of the egg shell, and conventional 4D microscopy induces too much phototoxicity at the rates and durations necessary for prolonged, blur-free imaging.

Here we report an approach that addresses these problems, and that allows inspection of neurodevelopmental decisions in live nematode embryos. First, we designed *i*SPIM, an adaptable module that adds plane illumination functionality to any inverted microscope base. This technical advance allowed us to continuously image the nematode embryo, scanning volumes every 2 s for the entire 14 h of embryogenesis with no detectable phototoxicity. Second, we merged two-color *i*SPIM with automated lineaging techniques to identify cells of interest and visualize their neurodevelopmental dynamics. We investigated four neurons expressing transcription factor CEH-10/Chx10 during early embryogenesis: CANL, CANR, RMED, and ALA. We then examined the cell migration and neurite outgrowth decisions made by these neurons throughout embryogenesis. We found that CANs use somal translocation and amoeboid movement as they translocate to their final position. We also visualized axon guidance and growth cone dynamics as neurites circumnavigate the nerve ring and the body of the worm to reach their targets. Measurement of these events was largely inaccessible before our approach. Our experiments demonstrate the power of *i*SPIM to facilitate inspection of live neurodevelopmental events, and pave the way for a 4D dynamic neurodevelopmental atlas in *C. elegans*.

Author contributions: G.R., Z.B., D.C.-R., and H.S. designed research; Y.W., A.G., and H.S. performed research; R.C., Z.B., and D.C.-R. contributed new reagents/analytic tools; Y.W., A.G., R.C., A.S., Z.D., Z.B., D.C.-R., and H.S. analyzed data; and Y.W., Z.B., D.C.-R., and H.S. wrote the paper.

The authors declare no conflict of interest.

*This Direct Submission article had a prearranged editor.

[1]To whom correspondence should be addressed. E-mail: yicong.wu@gmail.com.

[2]Z.B., D.-C.R., and H.S. contributed equally to this work.

This article contains supporting information online at www.pnas.org/lookup/suppl/doi:10.1073/pnas.1108494108/-/DCSupplemental.

Results

Development of *i*SPIM. Most of the neurodevelopmental decisions in *C. elegans* are made during embryonic neurulation (3, 24). This ontogenic time has remained largely inaccessible for two reasons: (*i*) Neurulation in the embryo is accompanied by fast movement and twitching, requiring faster volumetric imaging rates to avoid the artifacts induced by motion blur. (*ii*) Conventional 4D imaging technologies such as point-scanning confocal or two-photon microscopies fail to provide the necessary signal rates. Even if such point-scanning technologies are parallelized, as in spinning-disk or swept-field microscopy, the photodamage induced by continuous high-speed imaging results in developmental defects or arrest. To overcome these hurdles, we sought a fast, minimally invasive microscopy technique suitable for routine use in nematode embryos.

Light sheet-based fluorescence microscopy (LSFM) (25–28) employs parallelized excitation and a perpendicular detection geometry (29) for optically sectioned volumetric interrogation of living samples, thus enabling the study of in toto development (30) or neuronal dynamics (28) at high frame rates while reducing photodamage and photobleaching to levels far below other microscopy techniques. In most implementations (31), the LSFM system is designed around the specimen, requiring novel sample preparation (often embedding the sample in an agarose gel) and precluding the use of conventional sample mounts, such as glass coverslips. We designed *i*SPIM, a module that offers the advantages of plane illumination while maintaining the flexibility and sample geometry of commercially available inverted microscopes (Fig. 1, *Materials and Methods*, *SI Materials and Methods*, and Fig. S1).

*i*SPIM replaces the illumination pillar of an inverted microscope with a mechanical housing for two objectives that illuminate the sample with a light sheet (excitation), and collect the resulting fluorescence (detection). By rapidly translating the light sheet through the sample, the module enables rapid volumetric image collection without requiring specimen movement, similar to previous methods (28). The choice of objectives is mechanically constrained by the need to place them in the 90° orientation required for LFSM, without steric interference with each other or the sample. We thus chose two high NA (0.8), long working distance (3.5 mm), water-immersion (minimizing aberrations due to refractive index mismatch) objectives that satisfied this condition. The objective housing is attached to an automated linear translation stage so that the two objectives may be properly positioned relative to the sample. Samples are mounted on a rectangular coverslip (Fig. S2), and may be translated using an automated 3D mechanical stage and additionally imaged using the conventional light path built into the inverted microscope frame. In the experiments we describe herein, the conventional light path was particularly useful for rapidly finding embryos of appropriate age (e.g., two-cell stage) before *i*SPIM imaging.

Although *i*SPIM is compatible with a variety of live samples, we optimized our experiments for *C. elegans* embryogenesis by focusing the excitation light sheet to a beam waist of ~1.2 μm at the center of the embryo, thus minimizing diffractive spreading at the edges of our field of view (where we measured a beam waist of ~3 μm). The resulting spatial resolution, as measured on 100-nm beads embedded in a 2% agarose gel, was 0.52 ± 0.02 μm laterally and 1.70 ± 0.39 μm axially (n = 10 beads, measured over our ~30 × 50 μm field of view), similar to measurements carried out by others at similar N.A. (32). By rapidly scanning the light sheet in the focal plane (33) (*SI Materials and Methods* and Fig. S3), we mitigated striping artifacts that result from absorption in the sample plane.

High-Speed *i*SPIM Imaging of GFP-Histones in *C. elegans* Embryos from the Two-Cell Stage Until Hatching. We demonstrated the utility of *i*SPIM for live samples by imaging transgenic *C. elegans* embryos labeled with GFP-histone markers. Because *C. elegans* has an invariant cell lineage, and disruptive phototoxic perturbations do not result in cell lineage compensation, embryos provide a stringent assay for the potentially phototoxic effects of in vivo imaging (34). Furthermore, strains carrying GFP-histone markers have been well characterized by spinning disk microscopy, enabling direct comparison of the potential gains of *i*SPIM relative to this more workhorse technology (35). As in previous experiments, imaging GFP-histone–labeled *C. elegans* embryos with spinning-disk confocal microscopy (SDCM) was limited to a rate of ~1 vol/min from two cells until twitching (Movie S1 and *SI Materials and Methods*), as significantly higher imaging frequencies or longer durations at this frequency resulted in embryonic arrest due to phototoxicity (36). Imaging the same samples with our *i*SPIM module allowed continuous volumetric image collection every 2 s from the two-cell stage until hatching (Movie S2), a rate 30× faster than SDCM and close to the hardware limit imposed by our camera. Despite our much higher temporal sampling, we did not detect any obvious abnormalities in the imaged embryos in terms of morphology or in the timing of developmental hallmarks, such as the invariant order and orientation of blastomere divisions, gastrulation, pharyngeal shape, elongation, and twitching. Furthermore, embryos imaged with *i*SPIM hatched at the expected time (measured temporal variation within 5%, similar to previous studies) (34, 37) into viable larva stage 1 (L1) animals (Fig. 2*A* and Movie S2). *i*SPIM thus enabled the noninvasive collection of ~25,000 volumetric datasets over the entire 14-h period of nematode embryogenesis.

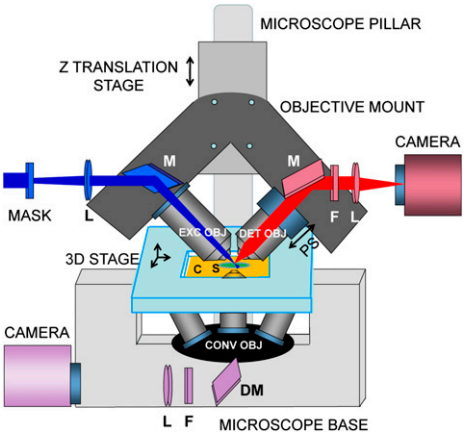

Fig. 1. *i*SPIM, plane illumination on an inverted microscope base. Two water-immersion objectives are mounted onto a Z translation stage that is bolted directly onto the illumination pillar of an inverted microscope. The demagnified image of a rectangular slit (MASK) is reimaged with lenses (L) and excitation *i*SPIM objective (EXC OBJ), thus producing a light sheet at the sample (S). For clarity, relay lens pairs between L and EXC OBJ are omitted in this schematic, but are included in Fig. S1. Sample fluorescence is detected (DET OBJ) using appropriate mirrors (M), emission filters (F), lenses (L), and camera. EXC OBJ is fixed in place and the light sheet is scanned through the sample using a galvanometric mirror (not shown). A piezoelectric objective stage (PS) moves DET OBJ in sync with the light sheet, ensuring that detection and excitation planes are coincident. The sample S is mounted onto a coverslip (C) that is placed onto a 3D translation stage, thus ensuring correct placement of S relative to *i*SPIM objectives. S may also be viewed through objectives (CONV OBJ), dichroic mirrors (DM), and optics in the conventional light path of the inverted microscope.

Despite the 30-fold increase in speed, raw *i*SPIM images displayed similar signal-to-noise ratio (SNR) to SDCM, and SNR could be further increased with deconvolution (Fig. S4). To assess the value of *i*SPIM for in toto cell biological studies, we imaged single dividing cells in the intact embryo and compared the spatiotemporal resolution of *i*SPIM and SDCM (Fig. 2*B*). Chromosome condensation and the kinetics of cytokinesis were clearly visible using *i*SPIM, but obscured in similarly nonperturbative SDCM.

Development of Two-Color *i*SPIM for Coupled Cell Identity Lineaging and Neurodevelopmental Imaging. During the first 14 h of development, the *C. elegans* embryo develops from a single-cell

DEVELOPMENTAL BIOLOGY

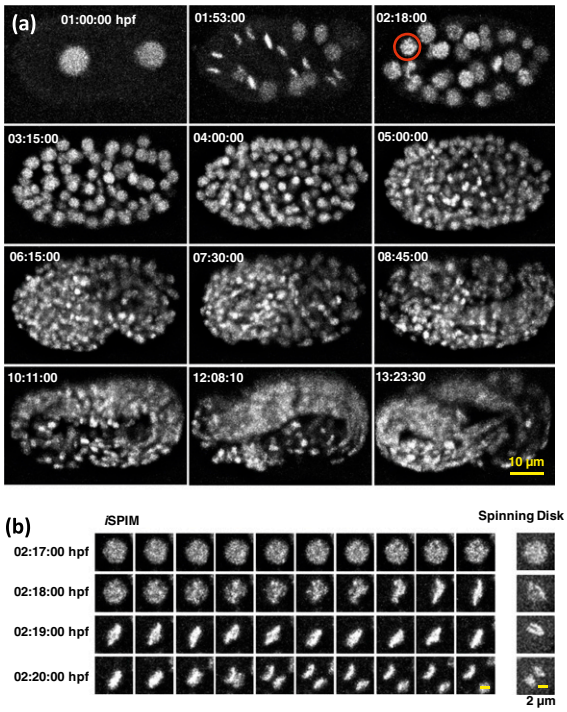

Fig. 2. High-speed nuclear imaging in the nematode embryo. Embryos with GFP-histones were volumetrically imaged at 30 vol/min from the two-cell stage until hatching. (*A*) Selected maximum-intensity projections from a representative embryo, highlighting different developmental stages (Movie S2). (Scale bar: 5 μm.) (*B*) Highlighted nuclei (circled in red, *A Top Right*) comparing maximum-intensity projections between *i*SPIM (*Left*, images sampled every 2 s but shown every 6 s due to space constraints) and spinning-disk confocal microscopy (*Right*, images sampled every minute, taken on a different embryo).

zygote to a 558-cell larva through an invariant cell lineage, where lineage identity equates with the fate of the cell (34, 35). Because of the invariant cell lineage of the nematode, *C. elegans* has long been a workhorse in the identification of transcription factors that instruct neuronal identity and development (5, 6, 38). We reasoned that the imaging rates afforded by *i*SPIM provided an opportunity to determine nuclear positions while also visualizing the expression pattern of transcription factors; this would allow us to simultaneously achieve two goals: (*i*) identification of neurons expressing the transcription factor and (*ii*) visualization of their neurodevelopmental dynamics.

To simultaneously image neurons and nuclei, we developed a worm strain that expressed histone:mCherry under a ubiquitous promoter, and GFP under the CEH-10/Chx10 promoter. The homeodomain transcription factor CEH-10 is a conserved regulatory transcription factor that affects the differentiation and development of a subset of neurons in *C. elegans* (15, 39, 40). Therefore, *ceh-10p*:GFP transgenic worms enable visualization of neurons that express this transcription factor. By alternately exciting the embryos with 488-nm and 561-nm lasers and capturing both GFP and mCherry fluorescence, we achieved two-color *i*SPIM at 12 vol/min (Fig. 3*A*, Movie S3, and *SI Materials and Methods*).

Lineage identity of cells expressing *ceh-10p*:GFP has been previously determined by longitudinal studies in fixed embryos, or by visualizing live embryos at specific time points (39, 40). Using *i*SPIM, we (*i*) recorded the dynamic GFP expression pattern of the *ceh-10p*:GFP strain; (*ii*) used the histone:mCherry signals to obtain the embryo lineage with the automated lineage tracing software, StarryNite (35, 41) (*SI Materials and Methods*); and (*iii*) correlated lineage with cytoplasmic expression pattern to identity the four brightest cells expressing *ceh-10p*:GFP (Fig. 3*C*). By 6 h postfertilization (hpf), GFP expression appeared in precursor cell ABalapppaa (bean stage of embryonic development), and subsequently in the daughter cells ALA (ABalapppaaa) and RMED (ABalapppaap; Fig. 3*A*). GFP expression was also subsequently observed in the canal-associated neurons, CANR (ABalappappa) and CANL (ABalapaaapa; Fig. 3*A*). The observed pattern of *ceh-10p*:GFP expression in these neuronal cells, and their subsequent migration through the onset of early twitching (~7:10:00 hpf, twofold stage), was reproducible across all 12 inspected embryos and is summarized as a cartoon model (Fig. 3*B*). Having established cell identity and initial migrations, we subsequently used a combination of one- and two-color *i*SPIM for more detailed analysis of the developmental dynamics of these neurons, from the comma stage through twitching.

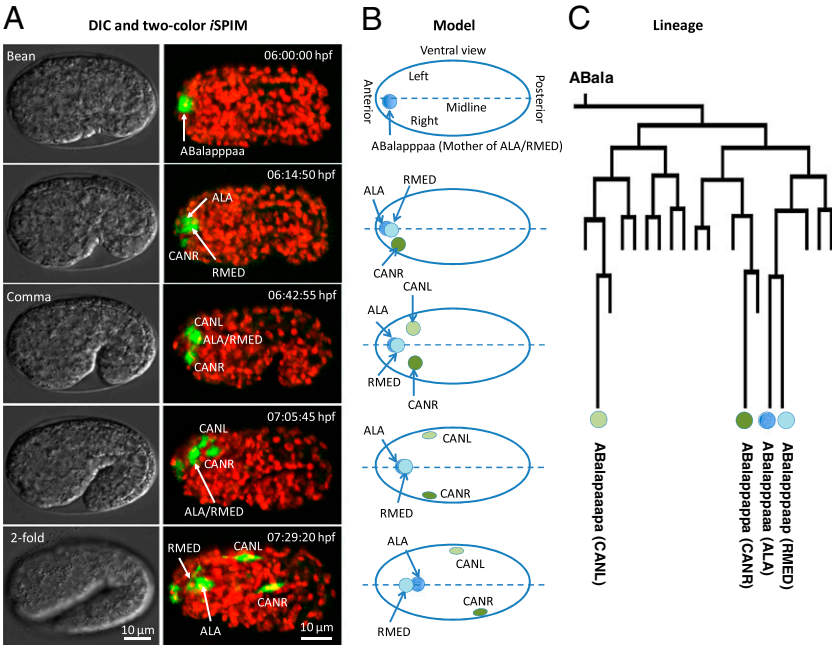

Fig. 3. Dual-color *i*SPIM and lineaging identifies neuronal cells expressing CEH-10/Chx10. (*A*) DIC and *i*SPIM maximum-intensity projections at indicated time points, highlighting ubiquitously expressed histone:mcherry (red) and *ceh-10p*:GFP (green) at selected times points. *i*SPIM images are from a representative embryo; DIC pictures were taken on a different animal and are provided only as a reference (Movie S3). (*B*) Cartoon model to accompany *A*, also emphasizing location of neurons with respect to the anatomical body plan of the embryo. (*C*) Computer-derived lineage tree for the identified neurons in *A*.

CAN Migration. Most cells in *C. elegans* undergo short migrations to reach their final positions (34). A few cells, such as the CANs, embark upon long-range migrations during development (Fig. 3*B*) (13, 34). Previous genetic analysis of CAN migration used the osmoregulatory phenotypes resulting from CAN dysfunction, and end-point analysis of CAN position, to identify molecules required for cell migration (10, 15). These studies resulted in fundamental insights regarding conserved molecular mechanisms of neuronal migration in vivo, further underscoring the value of the nematode system in neurodevelopment and gene discovery. Despite its importance as an experimental system for understanding cell migration, CAN migration in embryos has never been fully described, likely because of the limitations of conventional imaging methods.

Using *i*SPIM, we visualized CAN development in seven wild-type embryos, and observed that their neurodevelopmental progression is stereotyped across individual animals (Fig. 4*A* and Movie S4). CANs use multiple strategies as they navigate the different cellular environments in the nematode to reach their target destination. From 6:30:00 to 7:10:00 hpf, CANs slowly migrate longitudinally and posteriorly, traveling ∼10 μm from their birth site where fluorescence was first observed (Fig. 4*B*). From 6:30:00 to 6:45:00 hpf, migration is passive, likely resulting from cells moving en masse, as the relative positions of the CANs with respect to neighboring nuclei do not significantly change, and their migration rate of 0.15 μm/min is similar to neighboring neurons ALA and RMED (Fig. 4*A*).

From 6:45:00 to 7:10:00 hpf, CANs speed up slightly, moving at an average rate of 0.3 μm/min (Fig. 4*C*). In this interval immediately preceding twitching, CAN morphology changed from a spherical to a bipolar shape (yellow box in Fig. 4*A*; also, dual-color example in Fig. 4*D*), oriented along the anterior/posterior axis and along the direction of migration. The bipolar morphology was characterized by a lamellipodial structure, similar to a pseudopod, in the posterior side of the CANs, and a trailing process in the anterior side of the cell. During this active migratory phase we observed somal translocation of CANs and amoeboid movement (Fig. 4 *D* and *E*).

After ∼7:10:00 hpf, CANs preserved their bipolar morphology and appeared to move more rapidly in an amoeboid fashion (Fig. 4*E*) as they continued their migration toward the posterior end of the embryo (Fig. 4*A*). This period of active CAN migration coincides with embryonic twitching (jagged lines in Fig. 4*C*). Despite the large embryonic movements during twitching, we successfully tracked both CANs, finding that cells moved ∼20 μm in 30 min, an average speed of 0.7 μm/min until the end of migration at ∼7:45:00 hpf.

Characterization of Neurite Outgrowth Through Embryonic Twitching. CAN migration occurs during neurulation. During this same period, most neurons in the nematode simultaneously extend their neurites to reach their target regions (3, 24, 34). Although growth cone morphology in the embryonic ventral nerve cord has been described by fixing embryos at different developmental time points and visualizing axon outgrowth by EM (24), continuous neurite outgrowth during neurulation can now be documented in vivo for *C. elegans* embryos, along with descriptions of axon outgrowth as neurites circumnavigate the nerve ring.

To examine navigation around the nerve ring, we visualized neurite outgrowth in the ALA neuron (Fig. 5 *A* and *B* and Movie S5). Serial EM reconstructions of the nematode nerve ring show that in the adult, the ALA neuron is positioned in the dorsal ganglion behind the nerve ring and has two bilaterally symmetric neurites (3). These neurites enter the nerve ring, circumnavigate it, and exit laterally to project toward the posterior of the animal. Visualization of ALA outgrowth with *i*SPIM revealed the evolution of this process in vivo, and confirmed that ALA outgrowth was stereotyped across individual animals (four embryos inspected).

ALA neurite extension commenced at ∼6:40:00 hpf. Extension occurred simultaneously in the two bilaterally symmetric neurites extending from the anterior end of the ALA cell body (Fig. 5*A*). We observed that growth cones project from both left and right sides of the single ALA cell (Fig. 5*B*). As the neurites grow ventrally, circumnavigating the nerve ring, we found that ALA growth cones display dynamic exploratory behaviors. In all inspected embryos, at ∼7:20:00 hpf, the ALA growth cone bifurcates (Fig. 5*B*). During bifurcation, extension pauses for ∼10 min, after which the growth cone readopts its unipolar, unbranched morphology and continues navigation. We hypothesize that these bifurcations represent guidance decisions as ALA navigates and turns in the nerve ring. This hypothesis is based on the following observations: (*i*) pause sites in neurite outgrowth occurred at similar developmental times in different embryos, suggesting they are part of the developmental program; (*ii*) pause sites occurred at similar locations in the nerve ring of all embryos; and (*iii*) the locations where growth cones pause and bifurcate correspond to sites where the ALA neuron makes turning decisions in the nerve ring.

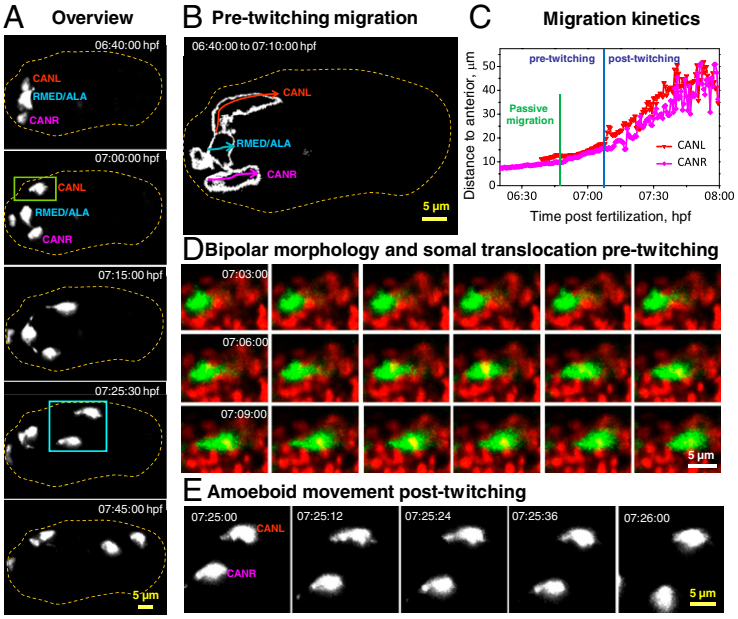

Fig. 4. Neuronal morphology and migration through early twitching. (*A*) Selected maximum-intensity projections of *ceh-10p*::GFP, highlighting migration of neurons after expression of GFP, through onset of early twitching. The outline of the embryo is indicated by the dotted line. (*B*) Outlines of the migratory path of individual neurons before embryonic twitching. (*C*) Migration kinetics of CANs from the dataset shown in *A*, through early twitching. 3D displacements are measured from the anterior tip of the embryo. (*D*) An example of somal translocation before twitching from a dual-color *i*SPIM dataset. (*E*) Higher-magnification view of the blue boxed region in *A*, showing amoeboid movement of CANs posttwitching as neurons migrate posteriorly. Dual-color images in *D* were acquired from a representative embryo at 12 vol/min; single-color images for other panels were acquired from another representative embryo at 10 vol/min (Movie S4). In all images, anterior is *Left* and posterior *Right*.

DEVELOPMENTAL BIOLOGY

We also visualized CAN outgrowth through embryonic twitching (Fig. 5 *C* and *D* and Movie S6). CANs cease to actively migrate 8 hpf. During the next hour, CANs retain their bipolar morphology, but do not extend a neurite. However, at 9 hpf, we observed the formation of anterior neurite extensions (Fig. 5*C*). These extensions persisted throughout the remainder of embryogenesis and eventually developed into growth cones. Growth cone biogenesis was observed as a flattened lamellar structure ~4-μm thick at the tip of the outgrowing neurite (Fig. 5*D*, orange stars). Outgrowth of the growth cones reaches speeds of 0.18 μm/min (Fig. 5*E*) and followed a similar trajectory anteriorly, in contrast to the previous, posterior cell migration trajectory taken by the CAN (Fig. 4). Neurite length in the CANs extended until it reached ~44 μm and the anterior part of the head of the worm. In addition to the anterior neurite, *i*SPIM also revealed the outgrowth of the dimmer, posterior CAN neurite (Fig. 5*F*). Posterior neurite outgrowth became visible ~12–13 hpf, after anterior neurite extension to the head of the nematode. Although posterior neurite outgrowth commences toward the end of embryogenesis, it does not conclude until after the animal hatches (L1 larva stage).

Discussion

Progress in the field of neurodevelopmental biology has been tightly linked to innovations in imaging technologies, and we believe *i*SPIM will be of great value in visualizing the neurodevelopmental dynamics that allow innervation of the nematode nervous system. To exemplify the value of *i*SPIM, we identified and described the cell migration and neurite outgrowth decisions made by a subset of cells, in vivo and with subcellular spatial resolution. CAN neurodevelopment was visualized for ~7 h from birth near the nose of the worm, subsequent migratory behaviors, and the extension of posterior and anterior neurites. Continuous, volumetric imaging allowed qualitative observations of the cell biological events through cell migration and axon guidance, as well as detailed quantification of the outgrowth kinetics in the twitching embryo. Our high imaging rate also allowed us to visualize ALA neurites as they circumnavigated the nerve ring.

*i*SPIM allows inspection of developmental events that were previously inaccessible, but significant room for technical improvement remains. Although our light sheet thickness was optimized for *C. elegans* embryos, resulting in better axial resolution than other experiments on larger samples (27, 30), the sheet was still created from a Gaussian beam. Gaussian beams undergo significant diffraction at increasing distances from the beam waist, coupling the quality of optical sectioning to the field of view and degrading the effective axial resolution at the sample edges. Exciting a fluorescent sample with scanned Bessel beams in an LSFM geometry (42) mitigates this problem and can markedly improve axial resolution, as has been demonstrated on single cells (43). Such a resolution improvement comes at a cost, however, as sidelobes in the Bessel beam profile cause significant out-of-plane illumination. Removing the contaminating effects of the sidelobes requires either a structured illumination approach (necessitating more images per plane, and thus exposing the sample to even more excitation) or multiphoton excitation (potentially leading to nonlinear photobleaching and photodamage).

A better alternative for improving axial resolution may be to collect fluorescence from multiple directions while maintaining the perpendicular LSFM geometry. Fusing the result of datasets taken at each view into a multiview image results in more isotropic resolution (44). This approach has typically been implemented by keeping illumination and detection directions fixed, while rotating the sample so that multiple views may be obtained. Rotating the sample is likely too slow for maintaining the high imaging rates we present here. We note that the benefits of multiview imaging may be realized with *i*SPIM, and at high speed, by leaving the sample fixed and performing alternate excitation and detection with both LSFM objectives, instead of using one objective for excitation and the other for detection, as presented herein. This scheme would provide two views, but a third could be added by using the conventional objective (Fig. 1) mounted in the inverted microscope base (45).

While inspecting the neurodevelopment of CEH-10–expressing cells, we found that migration and outgrowth are highly stereotyped across embryos. *i*SPIM in combination with the stereotypy of nematode embryonic development thus provides a unique opportunity to document the 4D wiring decisions of nervous system assembly. Because two-color *i*SPIM enables simultaneous identification of cells and inspection of their developmental dynamics, understanding the neurodevelopment of specific neurons in the context of neighboring cells and tissues is

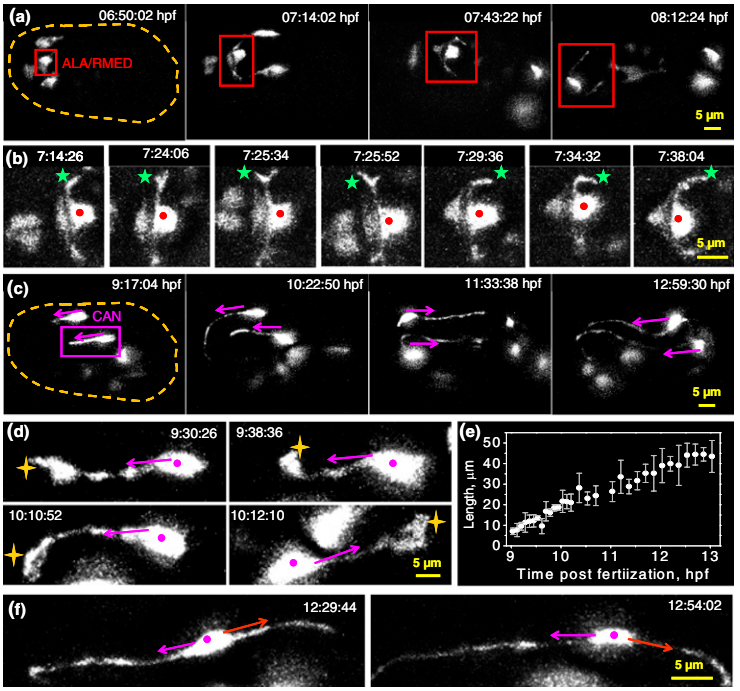

Fig. 5. Neuronal outgrowth through twitching. (*A*) Selected maximum-intensity projections emphasizing ALA neurite outgrowth from a representative embryo. The outline of the embryo is indicated by the dotted line. The red boxed region highlights ALA (Movie S5). (*B*) Higher-magnification view. The red dot marks ALA soma; the green star marks the *Left* neurite outgrowth. (*C*) Selected projections emphasizing CAN neurite outgrowth, from the same embryo as in *A* and *B* (Movie S6). Purple arrows highlight direction of outgrowth. Note that as the embryo is twitching inside the egg case, the relative position of the CANs inside the embryos changes between volumes. High-speed volumetric imaging through *i*SPIM enabled visualization of outgrowth through twitching with no motion blur. (*D*) Higher-magnification view, emphasizing growth cones (orange stars). (*E*) Quantification of anterior extensions (distance from center of cell body to tip of axon) over time, measured from four animals. Data were acquired at 30 vol/min. (*F*) Higher-magnification view of outgrowth of both anterior (pink arrows) and posterior (red arrows) CAN neurites, from the same embryo as in *A*–*D*. The posterior outgrowth became visible ~12–13 hpf.

now possible. Further improving the axial resolution of *i*SPIM in combination with cell-specific promoters or photoactivatable markers will enable the construction of a 4D dynamic brain atlas in the *C. elegans* embryo, thus providing a systems-level understanding of neurodevelopment.

Materials and Methods

Worm Strains. Worms were raised at 20 °C on nematode growth medium seeded with *E. coli* OP50. Strain BV24 [ltIs44 [pie-1p-mCherry::PH(PLC1delta1) + unc-119(+)]; zuIs178 [(his-72 1kb::HIS-72::GFP); unc-119(+)] V] was used to image nuclei. Strain BV117 [lqIs4 [ceh-10 promoter::GFP + rol-6(su1006)]; itIs37 [pie-1 promoter::mCherry::H2B::pie-1 3′ UTR + unc-119(+)]; stIs10226 [his-72 promoter::HIS-24::mCherry::let-858 3′ UTR + unc-119(+)]] was used for visualizing neuronal cells and processes. Preparation of worm embryos for *i*SPIM is discussed in detail in *SI Materials and Methods*.

Instrumentation. An Olympus IX-81 inverted fluorescence microscope served as the base for *i*SPIM experiments. We removed the illumination pillar of the microscope and modified it for mounting *i*SPIM excitation/detection objectives above the sample (Fig. 1). Mounting two high-N.A. objectives in a 90° orientation and in proper placement with respect to the sample is nontrivial, so we designed a custom objective mount for this function. The mount was bolted onto an automated translation stage (LS50; Applied Scientific Instrumentation) for correct positioning of the assembly in Z, and the combined mount/stage was bolted onto the modified illumination pillar. Both the modified illumination pillar and objective housing may be obtained from Applied Scientific Instrumentation. The objective mount also housed a fast piezoelectric objective positioner (PIFOC-P726; Physik Instrumente) that allowed us to move the *i*SPIM detection objective in sync with the light sheet, thus ensuring coincidence of excitation and detection planes. Further details on *i*SPIM excitation/detection optics and the power levels used during experiments are covered in *SI Materials and Methods*.

We also added an automated XY stage equipped with a Z piezo (PZ-2000; Applied Scientific Instrumentation) to the microscope base, for translating the sample to the focal/imaging plane of the *i*SPIM excitation/detection objectives. Rectangular coverslips containing the sample were placed in an autoclavable stainless steel rectangular chamber with removable bottom (I-3078-2450; Applied Scientific Instrumentation), and sealed in place with an O-ring (1.5-mm thickness, 40-mm inner diameter). This imaging chamber was placed into a temperature-controlled stage insert (Bioptechs, custom design) and the insert mounted to the PZ-2000 stage. Both the insert and imaging chamber were designed to allow unfettered access to both *i*SPIM objectives and to objectives that mount conventionally into the IX-81. Worm embryos were screened initially using a 10×, 0.3 N.A. air objective (1-U2B524; Olympus) and the 1.6× magnification expander internal to the microscope, using room lighting for illumination and an electron-multiplying CCD (EMCCD) camera (Andor iXon DU-885) mounted to the left side port of the microscope for detection.

ACKNOWLEDGMENTS. Support for this work was provided by the Intramural Research Programs of the National Institute of Biomedical Imaging and Bioengineering (Y.W., A.G., and H.S.), National Institutes of Health (NIH) Grant R00 NS057931 (to D.C.-R.), a fellowship from the Klingenstein Foundation, and Alfred P. Sloan Foundation Genetics Training Grant 5 T32 GM07499-34 (to R.C.). Z.B. was partly supported by NIH Grant R00 HG004643 and March of Dimes Basil O'Connor Starter Scholar Research Award 5FY09-526. A.S. was partly supported by NIH Grant F32 GM091874.

1. Jüttner R, Rathjen FG (2005) Molecular analysis of axonal target specificity and synapse formation. *Cell Mol Life Sci* 62:2811–2827.
2. Waites CL, Craig AM, Garner CC (2005) Mechanisms of vertebrate synaptogenesis. *Annu Rev Neurosci* 28:251–274.
3. White JG, Southgate E, Thomson JN, Brenner S (1986) The structure of the nervous system of the nematode *Caenorhabditis elegans*. *Philos Trans R Soc Lond* 314:1–340.
4. Jin Y (2002) Synaptogenesis: Insights from worm and fly. *Curr Opin Neurobiol* 12: 71–79.
5. Jukam D, Desplan C (2010) Binary fate decisions in differentiating neurons. *Curr Opin Neurobiol* 20:6–13.
6. Flames N, Hobert O (2009) Gene regulatory logic of dopamine neuron differentiation. *Nature* 458:885–889.
7. Silhankova M, Korswagen HC (2007) Migration of neuronal cells along the anterior-posterior body axis of *C. elegans*: Wnts are in control. *Curr Opin Genet Dev* 17:320–325.
8. Chisholm A, Tessier-Lavigne M (1999) Conservation and divergence of axon guidance mechanisms. *Curr Opin Neurobiol* 9:603–615.
9. Manser J, Roonprapunt C, Margolis B (1997) *C. elegans* cell migration gene mig-10 shares similarities with a family of SH2 domain proteins and acts cell non-autonomously in excretory canal development. *Dev Biol* 184:150–164.
10. Manser J, Wood WB (1990) Mutations affecting embryonic cell migrations in *Caenorhabditis elegans*. *Dev Genet* 11:49–64.
11. Forrester WC (2002) The Ror receptor tyrosine kinase family. *Cell Mol Life Sci* 59: 83–96.
12. Forrester WC, Dell M, Perens E, Garriga G (1999) A *C. elegans* Ror receptor tyrosine kinase regulates cell motility and asymmetric cell division. *Nature* 400:881–885.
13. Forrester WC, Garriga G (1997) Genes necessary for *C. elegans* cell and growth cone migrations. *Development* 124:1831–1843.
14. Forrester WC, Kim C, Garriga G (2004) The *Caenorhabditis elegans* Ror RTK CAM-1 inhibits EGL-20/Wnt signaling in cell migration. *Genetics* 168:1951–1962.
15. Forrester WC, Perens E, Zallen JA, Garriga G (1998) Identification of *Caenorhabditis elegans* genes required for neuronal differentiation and migration. *Genetics* 148: 151–165.
16. Fleming T, et al. (2010) The role of *C. elegans* Ena/VASP homolog UNC-34 in neuronal polarity and motility. *Dev Biol* 344:94–106.
17. Kim C, Forrester WC (2003) Functional analysis of the domains of the *C elegans* Ror receptor tyrosine kinase CAM-1. *Dev Biol* 264:376–390.
18. Blelloch R, Newman C, Kimble J (1999) Control of cell migration during *Caenorhabditis elegans* development. *Curr Opin Cell Biol* 11:608–613.
19. Branda CS, Stern MJ (1999) Cell migration and axon growth cone guidance in *Caenorhabditis elegans*. *Curr Opin Genet Dev* 9:479–484.
20. Hedgecock EM, Culotti JG, Hall DH (1990) The unc-5, unc-6, and unc-40 genes guide circumferential migrations of pioneer axons and mesodermal cells on the epidermis in *C. elegans*. *Neuron* 4:61–85.
21. Chan SS, et al. (1996) UNC-40, a *C. elegans* homolog of DCC (Deleted in Colorectal Cancer), is required in motile cells responding to UNC-6 netrin cues. *Cell* 87:187–195.
22. Culotti JG, Merz DC (1998) DCC and netrins. *Curr Opin Cell Biol* 10:609–613.
23. Quinn CC, Wadsworth WG (2008) Axon guidance: Asymmetric signaling orients polarized outgrowth. *Trends Cell Biol* 18:597–603.
24. Durbin RM (1987) Studies on the development and organization of the nervous system of *Caenorhabditis elegans*. PhD dissertation (Kings College, Cambridge, U.K.).
25. Voie AH, Burns DH, Spelman FA (1993) Orthogonal-plane fluorescence optical sectioning: Three-dimensional imaging of macroscopic biological specimens. *J Microsc* 170:229–236.
26. Fuchs E, Jaffe JS, Long RA, Azam F (2002) Thin laser light sheet microscope for microbial oceanography. *Opt Express* 10:145–154.
27. Huisken J, Swoger J, Del Bene F, Wittbrodt J, Stelzer EHK (2004) Optical sectioning deep inside live embryos by selective plane illumination microscopy. *Science* 305: 1007–1009.
28. Holekamp TF, Turaga D, Holy TE (2008) Fast three-dimensional fluorescence imaging of activity in neural populations by objective-coupled planar illumination microscopy. *Neuron* 57:661–672.
29. Stelzer EHK, Lindek S (1994) Fundamental reduction of the observation volume in far-field light microscopy by detection orthogonal to the illumination axis: Confocal theta microscopy. *Opt Commun* 111:536–547.
30. Keller PJ, Schmidt AD, Wittbrodt J, Stelzer EH (2008) Reconstruction of zebrafish early embryonic development by scanned light sheet microscopy. *Science* 322:1065–1069.
31. Huisken J, Stainier DY (2009) Selective plane illumination microscopy techniques in developmental biology. *Development* 136:1963–1975.
32. Engelbrecht CJ, Stelzer EHK (2006) Resolution enhancement in a light-sheet-based microscope (SPIM). *Opt Lett* 31:1477–1479.
33. Huisken J, Stainier DYR (2007) Even fluorescence excitation by multidirectional selective plane illumination microscopy (mSPIM). *Opt Lett* 32:2608–2610.
34. Sulston JE, Schierenberg E, White JG, Thomson JN (1983) The embryonic cell lineage of the nematode *Caenorhabditis elegans*. *Dev Biol* 100:64–119.
35. Bao Z, et al. (2006) Automated cell lineage tracing in *Caenorhabditis elegans*. *Proc Natl Acad Sci USA* 103:2707–2712.
36. Bao Z, Murray JI (2010) Live imaging of Caenorhabditis elegans embryogenesis. *Imaging in Developmental Biology: A Laboratory Manual*, eds Sharpe J, Wong R (Cold Spring Harbor Lab Press, Cold Spring Harbor, NY).
37. Schnabel R, Hutter H, Moerman D, Schnabel H (1997) Assessing normal embryogenesis in *Caenorhabditis elegans* using a 4D microscope: Variability of development and regional specification. *Dev Biol* 184:234–265.
38. Hobert O, Carrera I, Stefanakis N (2010) The molecular and gene regulatory signature of a neuron. *Trends Neurosci* 33:435–445.
39. Hawkins NC, McGhee JD (1990) Homeobox containing genes in the nematode *Caenorhabditis elegans*. *Nucleic Acids Res* 18:6101–6106.
40. Bertrand V, Hobert O (2009) Linking asymmetric cell division to the terminal differentiation program of postmitotic neurons in *C. elegans*. *Dev Cell* 16:563–575.
41. Santella A, Du Z, Nowotschin S, Hadjantonakis AK, Bao Z (2010) A hybrid blob-slice model for accurate and efficient detection of fluorescence labeled nuclei in 3D. *BMC Bioinformatics* 11:580.
42. Fahrbach FO, Simon P, Rohrbach A (2010) Microscopy with self-reconstructing beams. *Nat Photonics* 4:780–785.
43. Planchon TA, et al. (2011) Rapid three-dimensional isotropic imaging of living cells using Bessel beam plane illumination. *Nat Methods* 8:417–423.
44. Swoger J, Verveer P, Greger K, Huisken J, Stelzer EHK (2007) Multi-view image fusion improves resolution in three-dimensional microscopy. *Opt Express* 15: 8029–8042.
45. Dunsby C (2008) Optically sectioned imaging by oblique plane microscopy. *Opt Express* 16:20306–20316.

Supporting Information

Wu et al. 10.1073/pnas.1108494108

SI Materials and Methods

Sample Preparation. Rectangle no. 1.5 glass coverslips (24 × 50 mm; VWR, 48393–241) were incubated in 5:1:1 Milli-Q filtered H_2O: ammonium hydroxide:hydrogen peroxide for ∼10 h at 75 °C, serially rinsed in H_2O and methanol, and flamed. Parafilm (Parafilm-M; SPI Supplies) was placed onto cleaned coverslips to define a square ∼4 × 4 mm in the central portion of the coverslip (Fig. S2). The parafilm mask was adhered to the coverslip by heating at ∼70 °C for 5 min, and the resulting coverslips were stored dry until use. Immediately before adding embryos, coverslips were coated for ∼10 min with poly-D-lysine (1 mg/mL in H_2O; P4408-10MG; Sigma) to increase adherence to the coverslip.

Embryos were collected from gravid hermaphrodites as previously described (1). To save time and to ensure that embryos were at the two- to four-cell stage at the start of imaging, the preassembled coverslip was placed into the imaging chamber and covered with M9 before embryo extraction. Collected embryos were placed onto the central portion of the coverslip assembly (Fig. S2). To allow embryos to settle to the coverslip surface, we waited 2–3 min before transporting the imaging chamber to the *i*SPIM setup. Temperature was maintained at 20 °C during experiments using a temperature controlled stage insert (Bioptechs, custom design).

***i*SPIM Excitation Optics.** All optics were mounted on an optical table (TMC 784-659-02DR) to minimize mechanical vibrations. The output beam from a 100-mW 488-nm laser (Newport PC14963) was directed through an achromatic half-wave plate (Thorlabs WPH05M-488), an 8× beam expander (L1 and L2; Thorlabs LC1054-A and AC254-200-A-ML, f (focal length) = −25 mm and f = 200 mm), and an acousto-optic tunable filter (AOTF; Quanta Tech AOTFnC-400.650-TN) for power and shuttering control. The resulting beam was directed onto a galvanometric mirror (GALVO1; Thorlabs GVSM001) and imaged onto a rectangular slit with dimensions 600 μm × 12 mm (MASK, Photo Sciences) via a 5× cylindrical beam expander (CBE; Thorlabs LJ1125L2-A and LJ1653RM-A, f = 40 mm and f = 200 mm). GALVO1 was used to mitigate striping artifacts, discussed further herein. The resulting rectangular beam shape was reimaged onto the sample plane by lens pairs L3 and L4 (Thorlabs AC254-250-B-ML and AC254-100-B-ML, f = 250 mm and f = 100 mm); L5 and L6 (Edmund Optics and Thorlabs NT64-838 and AC254-100-B-ML, f = 90 mm and f = 100 mm); and L7 and the *i*SPIM excitation objective (Thorlabs and Nikon AC254-300-B-ML and MRD07420, f = 300 mm and f = 5 mm). A second galvanometric mirror (GALVO2, Thorlabs GVSM001) was placed at the front focal plane of L5, and served to translate the light sheet axially at the sample plane, thus defining the excitation volume. Each lens pair was placed in a 4f imaging configuration, such that the front focal plane of the lens in the preceding pair coincided with the back focal plane of the lens in the next pair, and lenses in each pair were separated by the sum of their focal lengths, resulting in a magnification of (100/250) × (100/90) × (5/300) = 7.4 × 10^{-3} between rectangular slit and sample plane. For dual-color experiments, we coupled a 200-mW, 561-nm laser beam into the excitation path (CrystaLaser CL561-200) via a dichroic mirror (DC; Semrock Di01-R488-25 × 36) after first passing the beam through an achromatic half-wave plate (Thorlabs AHWP05M-600). These elements are shown in Fig. S1 in two perpendicular views. We note that more compact geometries with fewer lens pairs are possible, but we found that the extra path length was helpful in directing the beam from the base of the optical table (where the laser was mounted) to the back focal plane of the *i*SPIM excitation objective (360 mm above the optical table).

Mitigating Striping in *i*SPIM. SPIM images are prone to striping or shadowing artifacts that arise from absorption in the plane of the light sheet (2). One method for alleviating such artifacts is to raster the angle of the light sheet so that regions of the sample that would otherwise be occluded by absorbers in the 0° direct beam path are induced to fluoresce by excitation from a different angle. We implemented this method by rastering GALVO1 over an angular range of ±7.5° at 250 Hz, and reimaging this rotation at the sample plane, thus altering the angle of the *i*SPIM excitation sheet and mitigating striping artifacts (Fig. S3).

***i*SPIM Detection.** Fluorescence was collected via the 0.8-N.A., 40× *i*SPIM detection objective, filtered through a long-pass filter (Semrock LP02-488RU-25) to reject 488-nm pump light, expanded 2.5× (Applied Scientific Instrumentation CM-2.5×), and imaged with a 200-mm tube lens onto a back-thinned electron-multiplying CCD (EMCCD; Andor iXon DU-897), operated at an EM gain of 300 and exposure time of 25 ms (the minimum possible exposure time operating in frame transfer mode at the ∼360 × 360 pixel field of view we used is ∼21 ms). The resulting image pixel size was 16 μm/(40 × 2.5) = 160 nm. For dual-color experiments, we added a notch filter (Semrock NF03-561E-25) to block 561-nm pump light.

Excitation Power and Energy Density. For 30 vol/min experiments on the BV24 GFP-histone line, we adjusted the 488-nm excitation power (measured after lens L7, before the *i*SPIM excitation objective) via the AOTF (Acousto-Optical Tunable Filter) to 13 μW for the first 90 min of measurement, and 5 μW for the remaining period (∼11.5 h). As the exposure time was half the imaging period (due to the readout speed of our camera), the total energy delivered to the embryo during the entire imaging period was ∼0.14 J, which corresponds to an energy density of ∼2.3 μJ/μm^3, considering a typical embryo size of ∼50 × 40 μm × 30 μm. Assuming 23,400 vol (13-h imaging period), this implies an energy of ∼6.0 μJ and energy density of 0.1 nJ/μm^3 per stack.

For the 30 vol/min measurements on the BV117 neuronal line, we adjusted the 488-nm excitation power to 7 μW over an 8-h imaging period and a total exposure time of 4 h. Thus, the total energy and energy density delivered to the embryo was ∼0.10 J and ∼1.7 μJ/μm^3, respectively. Because a total of ∼14,400 vol were collected, the energy and energy density for each stack were ∼6.9 μJ and 0.12 nJ/μm^3, respectively.

For the 12-vol/min dual-color experiments on the BV117 neuronal line, the excitation power for 488 nm and 561 nm were adjusted to 9 μW and 7 μW over a 7.5-h imaging period (with a 4.5-h total exposure time). The calculated total energy and energy density delivered to the embryo was ∼0.13 J and 2.2 μJ/μm^3, respectively. These values correspond to an energy of ∼24 μJ and energy density of 0.4 nJ/μm^3 per stack, as a total of 5,400 vol were imaged.

The energy and energy density values we used are near the threshold for on-time hatching. Exposing the embryos to more light introduced >5% variability in hatching time, or arrest during embryonic twitching. For comparable calculations on SDCM, see sections following.

Data Acquisition. Custom software was written in Labview (National Instruments) and used in conjunction with 16-bit DAQ cards (National Instruments PCI 6733 and PCI6115S) to control

and synchronize (*i*) the galvo that swept the excitation light sheet; (*ii*) the translation of the piezoelectric positioner containing the detection objective that imaged the excitation plane; and (*iii*) images obtained by the EMCCD camera. Two analog step-wise triangle waveforms were used to drive the galvanometric mirror and piezoelectric objective stage, respectively, and digital square waveforms were used for triggering the EMCCD and AOTF. Analog waveforms were synchronized with a digital trigger pulse and scaled appropriately (Stanford Research Systems, mainframe SIM900 and amplifier SIM983) before driving galvo and piezo. Software is available upon request from the authors.

In each 3D stack, 40 xy slices separated by a z step of 1 μm were imaged with a volume size of 360 × 360 × 40 pixels (width × length × depth), corresponding to an imaging volume of dimensions 57.6 × 57.6 × 40 μm. Each slice was acquired with an exposure time of 24–49 ms, resulting in an imaging time of 2–3 s/vol. The 3D imaging stacks were continuously recorded (7–14 h of embryonic development) and spooled directly to disk, resulting in datasets containing up to 1,008,000 images, or 25,200 recorded volumes (total file size up to ∼260 GB) over the lifetime of a single embryo.

For dual-color imaging, embryos were alternately excited (every other frame) with 488-nm and 561-nm lasers by controlling the AOTF shuttering with two digital pulse trains, issued from LabView. Each frame was acquired with an exposure time of ∼36.5 ms and readout time of ∼26 ms, resulting in an imaging time of 5 s/vol (40 frames per color for a total of 80 frames/vol).

Data Processing. Data processing was implemented in Matlab and ImageJ, and included cropping, deconvolution, and calculation of maximum-intensity projections. After initially examining the data by eye, a region of interest was selected and the data cropped, thus reducing unnecessary future computation. Each cropped 3D image stack was background subtracted and treated by the Richardson–Lucy deconvolution algorithm for enhancing contrast and reassigning out-of-focus fluorescence to its correct axial location. Deconvolution was implemented on a free package [École Polytechnique Fédérale de Lausanne (EPFL) DeconvolutionLab, ImageJ plug-in) with a TV regularization parameter of 0.001, an iteration number of 30, and a perfect point spread function theoretically identified by the N.A. of the detection objective lens (0.8) and the wavelength of the GFP fluorescence (515 nm; calculated using the "simple PSF" option in 3D_Deconvolution ImageJ plug-in developed at EPFL). Finally, to facilitate visualization and interpretation of the *i*SPIM data, maximum-intensity projections at each time point of the raw and deconvolved image stacks were calculated.

Image Analysis. Neurite data displayed in Fig. 5 were calculated by manually tracing neurite extensions in XY, XZ, and YZ projections from 3D volumetric images and calculating extension lengths using the Freehand Line Tool in ImageJ. The 3D contour length L_{3D} was calculated according to the formula $L_{3D} = [0.5 \times (L_{XY}^2 + L_{XZ}^2 + L_{YZ}^2)]^{0.5}$, where L_{XY}, L_{XZ}, and L_{YZ} are the extension lengths in each projection.

Cell lineage was traced based on nuclear mCherry signals using the StarryNite software as previously described (3). Errors in nuclear identification and tracking were corrected based on visual examination of the images using AceTree software (4, 5).

Spinning-Disk Confocal Microscopy. *C. elegans* 4D confocal images were acquired on a Zeiss Axio Observer.Z1 base equipped with a 491-nm laser (Spectral Applied Research, Laser Merge Model LMM5), a spinning-disk confocal system (Quorum Technologies, Quorum Wave FX), a 40× 1.3-N.A. PlanApo oil objective (Zeiss, 420762–9800-000), and an EMCCD (Hamamatsu). Embryos were mounted as previously described (6). Volumes were recorded at a temporal resolution of 1 min for embryos between the two-cell and twofold stages, with 30 planes/vol and an exposure time of 135 ms per plane. To normalize for loss of fluorescence in lower focal planes and the increase in fluorescence later in development, adjustments were made to laser power (ranging from 10 μW, for the first 125 min to 8 μW, for the last 325 min) during the imaging period. These settings resulted in a total energy and energy density of 0.016 J and 0.26 μJ/μm^3 during the imaging period. As a total of 450 vol were imaged, the per-stack energy and energy density are ∼35.6 μJ and 0.58 nJ/μm^3.

1. Bao Z, Murray JI (2010) Live imaging of *Caenorhabditis elegans* embryogenesis. *Imaging in Developmental Biology: A Laboratory Manual*, eds Sharpe J, Wong R (Cold Spring Harbor Lab Press, Cold Spring Harbor, NY).
2. Huisken J, Stainier DYR (2007) Even fluorescence excitation by multidirectional selective plane illumination microscopy (mSPIM). *Opt Lett* 32:2608–2610.
3. Santella A, Du Z, Nowotschin S, Hadjantonakis A-K, Bao Z (2010) A hybrid blob-slice model for accurate and efficient detection of fluorescence labeled nuclei in 3D. *BMC Bioinformatics* 11:580.
4. Boyle TJ, Bao Z, Murray JI, Araya CL, Waterston RH (2006) AceTree: A tool for visual analysis of *Caenorhabditis elegans* embryogenesis. *BMC Bioinformatics* 7:275.
5. Murray JI, Bao Z (2010) Automated lineage and expression profiling in live *Caenorhabditis elegans* embryos. *Imaging in Developmental Biology: A Laboratory Manual*, eds Sharpe J, Wong R (Cold Spring Harbor Lab Press, Cold Spring Harbor, NY), Vol 56.
6. Bao Z, Murray JI (2010) Live imaging of *Caenorhabditis elegans* embryogenesis. *Imaging in Developmental Biology: A Laboratory Manual*, eds Sharpe J, Wong R (Cold Spring Harbor Lab Press, Cold Spring Harbor, NY).

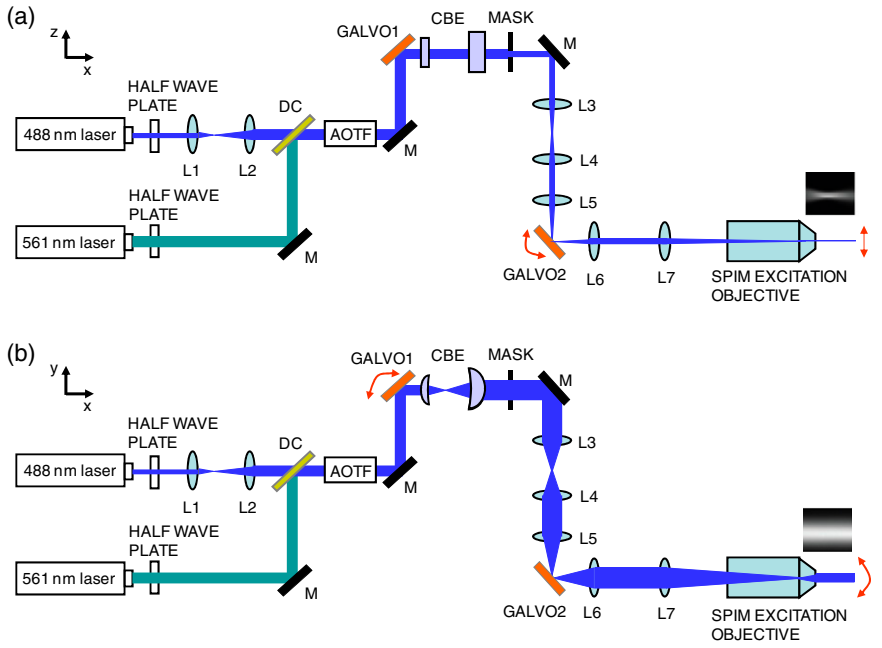

Fig. S1. Excitation optics for *i*SPIM. Laser 488 is beam expanded (L1 and L2) and combined with Laser 561 via a dichroic mirror (DC). Both lasers are directed through half-wave plates and an AOTF (for power control and shuttering) before further beam shaping by cylindrical beam expander (CBE) and rectangular slit (MASK). The CBE also images galvanometric mirror GALVO1 onto the rectangular mask; rotations of GALVO1 rotate the beam in the plane of the figure and serve to mitigate striping artifacts that occur in *i*SPIM (Fig. S3). Three telescope pairs (L3 and L4; L5 and L6; and L7 and the excitation objective), each in a 4f configuration, reimage the mask at the sample plane, thus creating a light sheet. A second galvanometric mirror (GALVO2) placed at the focal plane of L5 serves to translate the light sheet, enabling high-speed volumetric imaging at the sample plane. Not shown for clarity: periscopes that elevate the beam from the optical table surface into the *i*SPIM excitation objective and additional mirrors for beam alignment. Note that the figure is not to scale, and that views *A* and *B* are rotated 90° with respect to each other. See *SI Materials and Methods* for focal lengths of all lenses and further details.

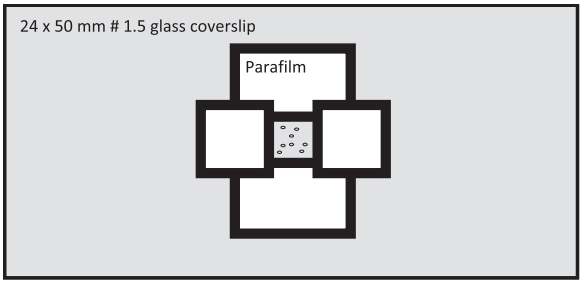

Fig. S2. Sample mounting. Parafilm (white) is cut and melted onto a cleaned 24 × 50 mm glass coverslip (gray). The parafilm encloses a 4 × 4 mm area in the center of the coverslip, where embryos (black dots) are deposited. The schematic is to scale; see *Materials and Methods* for further details.

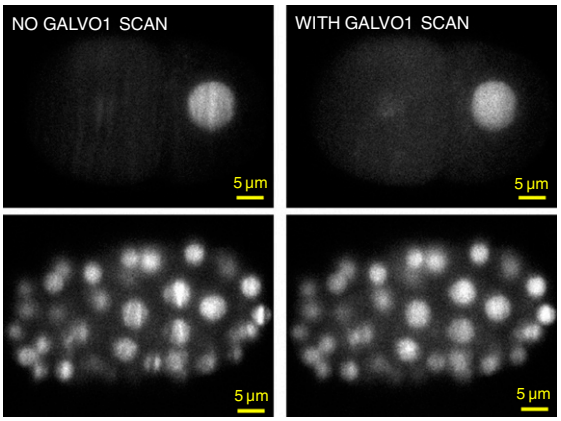

Fig. S3. Mitigation of striping artifacts in *i*SPIM. (*Left*) Single z slices from GFP-histone–expressing embryo at early (*Upper*) and later (*Lower*) time points. GALVO1 was held fixed. (*Right*) Same slices at *Left*, but now with GALVO1 rotating at 250 Hz, over a ±7.5° swing. Note the reduction in striping and shadowing.

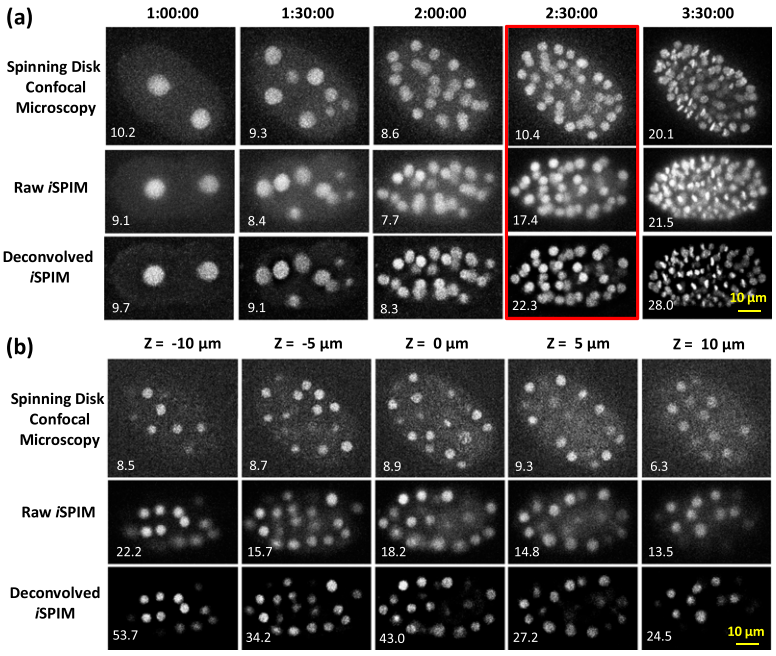

Fig. S4. Signal-to-noise ratio (SNR) comparison among spinning-disk confocal, raw *i*SPIM, and deconvolved *i*SPIM data. (*A*) Comparison between maximum-intensity projections at indicated time points (measured relative to fertilization). (*B*) Comparison between individual z slices for the time point outlined in red in *A*. SNR values, indicated at the *Lower Left* of each panel, were calculated by averaging pixel values in a region surrounding each nuclei, averaging these averaged nuclear pixel values, and dividing by the SD of the pixel values in an identically sized background region outside the embryo.

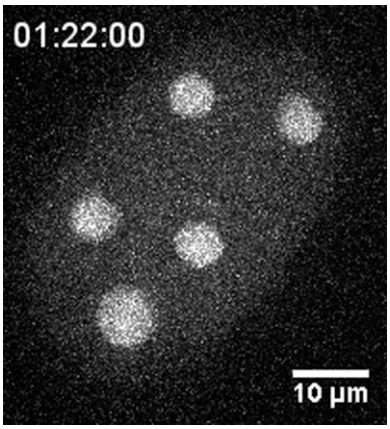

Movie S1. The BV24 GFP-histone line imaged with spinning-disk confocal microscopy at 1 vol/min. Maximum-intensity projections are displayed. Times are indicated from fertilization.

Movie S1

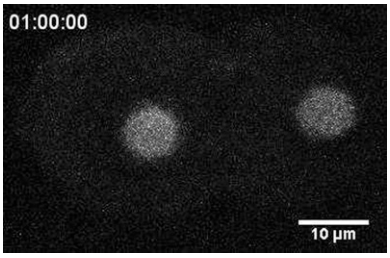

Movie S2. The BV24 GFP-histone line imaged with *i*SPIM at 30 vol/min from the two-cell stage until hatching. Maximum-intensity projections are displayed. Times are indicated from fertilization.

Movie S2

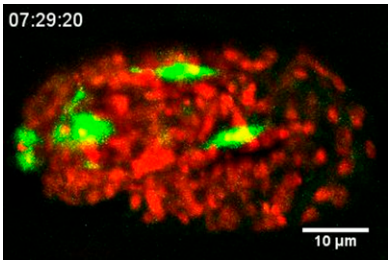

Movie S3. The *ceh-10* line imaged with two-color *i*SPIM at 12 vol/min, highlighting ubiquitously expressed histone:mcherry in red and *ceh-10p*:GFP in green. Maximum-intensity projections are displayed. Times are indicated from fertilization.

Movie S3

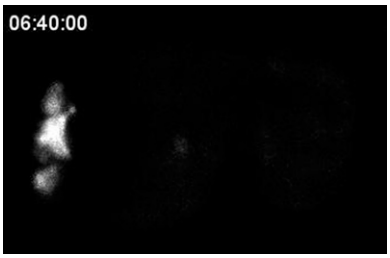

Movie S4. CAN neurodevelopment of the *ceh-10* line visualized with *i*SPIM at 10 vol/min. Maximum-intensity projections are displayed. Times are indicated as hours after fertilization.

Movie S4

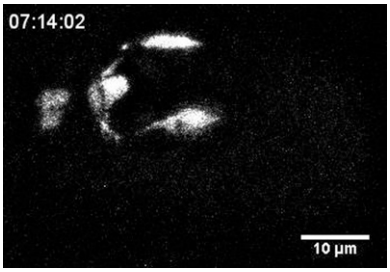

Movie S5. Neurite outgrowth in the ALA neuron of the *ceh-10* line visualized with *i*SPIM at 30 vol/min. Maximum-intensity projections are displayed. Times are indicated from fertilization.

Movie S5

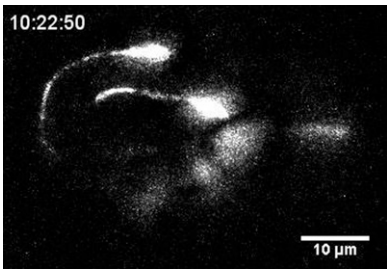

Movie S6. CAN neuronal outgrowth in the *ceh-10* line visualized through twitching with *i*SPIM at 30 vol/min. Maximum-intensity projections are displayed. Times are indicated from fertilization.

Movie S6